

Automated Identification of “Dunkelflaute” Events: A Convolutional Neural Network–Based Autoencoder Approach

BOWEN LI,^a SUKANTA BASU,^a AND SIMON J. WATSON^b

^a *Faculty of Civil Engineering and Geosciences, Delft University of Technology, Delft, Netherlands*

^b *Faculty of Aerospace Engineering, Delft University of Technology, Delft, Netherlands*

(Manuscript received 11 February 2022, in final form 7 August 2022)

ABSTRACT: As wind and solar power play increasingly important roles in the European energy system, unfavorable weather conditions, such as “Dunkelflaute” (extended calm and cloudy periods), will pose ever greater challenges to transmission system operators. Thus, accurate identification and characterization of such events from open data streams (e.g., reanalysis, numerical weather prediction, and climate projection) are going to be crucial. In this study, we propose a two-step, unsupervised deep learning framework [wind and solar network (WISRnet)] to automatically encode spatial patterns of wind speed and insolation, and subsequently, identify Dunkelflaute periods from the encoded patterns. Specifically, a deep convolutional neural network (CNN)–based autoencoder (AE) is first employed for feature extraction from the spatial patterns. These two-dimensional CNN-AE patterns encapsulate both amplitude and spatial information in a parsimonious way. In the second step of the WISRnet framework, a variant of the well-known k -means algorithm is used to divide the CNN-AE patterns in region-dependent meteorological clusters. For the validation of the WISRnet framework, aggregated wind and solar power production data from Belgium are used. Using a simple criterion from published literature, all the Dunkelflaute periods are directly identified from this 6-year-long dataset. Next, each of these periods is associated with a WISRnet-derived cluster. Interestingly, we find that the majority of these Dunkelflaute periods are part of only 5 clusters (out of 25). We show that in lieu of proprietary power production data, the WISRnet framework can identify Dunkelflaute periods from public-domain meteorological data. To further demonstrate the prowess of this framework, it is deployed to identify and characterize Dunkelflaute events in Denmark, Sweden, and the United Kingdom.

KEYWORDS: Renewable energy; Clustering; Deep learning

1. Introduction

With wind and solar power becoming major contributors to the European energy system, it is crucial to identify and characterize extreme weather events, which may significantly affect power production. Simultaneous low levels of wind and solar power production during Dunkelflaute events are causing increasing concern (Meinke-Hubeny et al. 2017; Wetzel 2017; Li et al. 2020, 2021a,b). These events occur several times each year, predominately during winter months, in northern European countries and sometimes last for several days (Li et al. 2021a). They can challenge transmission system operators in terms of balancing supply and demand of electricity. Therefore, a reliable way to identify, characterize, and eventually forecast Dunkelflaute events becomes a necessity.

One of the first peer-reviewed studies on Dunkelflaute was conducted by Li et al. (2021b). They investigated the capability of contemporary mesoscale models to simulate Dunkelflaute events. In a follow-up study (Li et al. 2021a), they documented a brief climatology of Dunkelflaute events for countries surrounding the North and Baltic Seas. They utilized aggregated power production data for the identification of Dunkelflaute cases. Owing to their proprietary nature, renewable power production data are often not easily accessible for research. Furthermore, due to the young age of the renewable energy industry, only a limited amount of historical power production data is available from most countries. In contrast, long-term

(ranging from mid-1800 to 2100), gridded meteorological data (e.g., reanalysis, numerical weather forecast, and climate projection) are readily available in the public domain. In the present study, we develop a machine learning (ML)–based approach that can ingest these types of open data streams, and in turn, can automatically identify Dunkelflaute events.

In recent years, ML algorithms have been widely used in many fields for learning intricate structures from large datasets (LeCun et al. 2015; Goodfellow et al. 2016). For example, in the field of Earth science, ML has been proven useful in numerous applications, such as cloud image classification (Shi et al. 2017; Zhang et al. 2018), land surface classification (Li et al. 2014), ozone profile shape estimation (Xu et al. 2017), and weather prediction (McGovern et al. 2017; Herman and Schumacher 2018; Rasp and Lerch 2018; Esteves et al. 2019). Moreover, ML techniques have shown their potential for identifying certain types of prominent weather patterns like tropical cyclones, fronts, and atmospheric rivers in large climate datasets (Liu et al. 2016; Racah et al. 2016). To the best of our knowledge, the present study is the first ML-based study of the Dunkelflaute phenomenon.

The rest of the paper is organized as follows. In section 2, we discuss a few ML algorithms that are relevant for the proposed wind and solar network (WISRnet) framework. The datasets used in the numerical experiments are described in section 3. In section 4, we delve into the WISRnet framework. Clustering and validation results are documented in section 5 followed by a summarized discussion in section 6. In-depth

Corresponding author: Bowen Li, B.Li-1@tudelft.nl

DOI: 10.1175/AIES-D-22-0015.1 e220015

© 2022 American Meteorological Society. For information regarding reuse of this content and general copyright information, consult the AMS Copyright Policy (www.ametsoc.org/PUBSReuseLicenses).

Unauthenticated | Downloaded 10/10/25 06:08 PM UTC

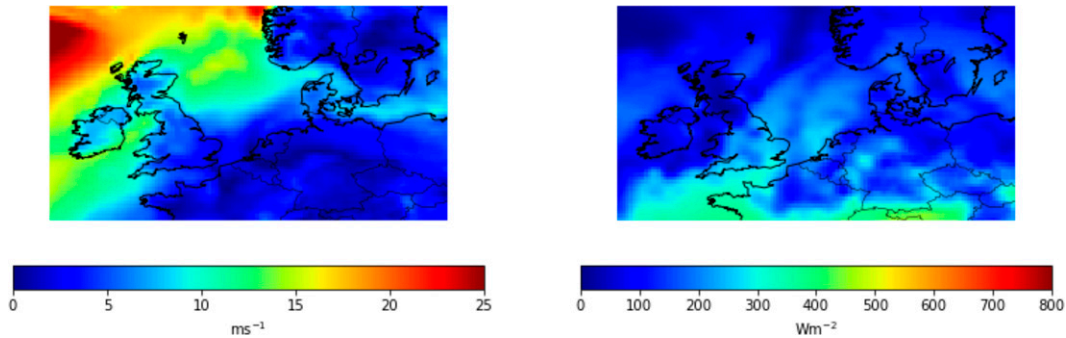


FIG. 1. Spatial fields of (left) 100-m wind speed and (right) downwelling shortwave radiation (insolation) at the surface at 1200 UTC 16 Jan 2017. On this day, a Dunkelflaute event occurred over Belgium causing a large shortfall in renewable power generation.

technical details and various sensitivity studies are reported in five appendices.

2. Overview of relevant machine learning algorithms

Machine learning refers to the automatic extraction of useful information or the learning of a specific task from

given input data (Shalev-Shwartz and Ben-David 2014). It has two basic forms: supervised and unsupervised learning. Supervised learning utilizes known inputs and corresponding labeled ground truth data (Kotsiantis et al. 2007). In contrast, unsupervised learning discovers groups of items in the data using unlabeled instances (Zanero and Savaresi 2004). In this research, given the unavailability of labeled

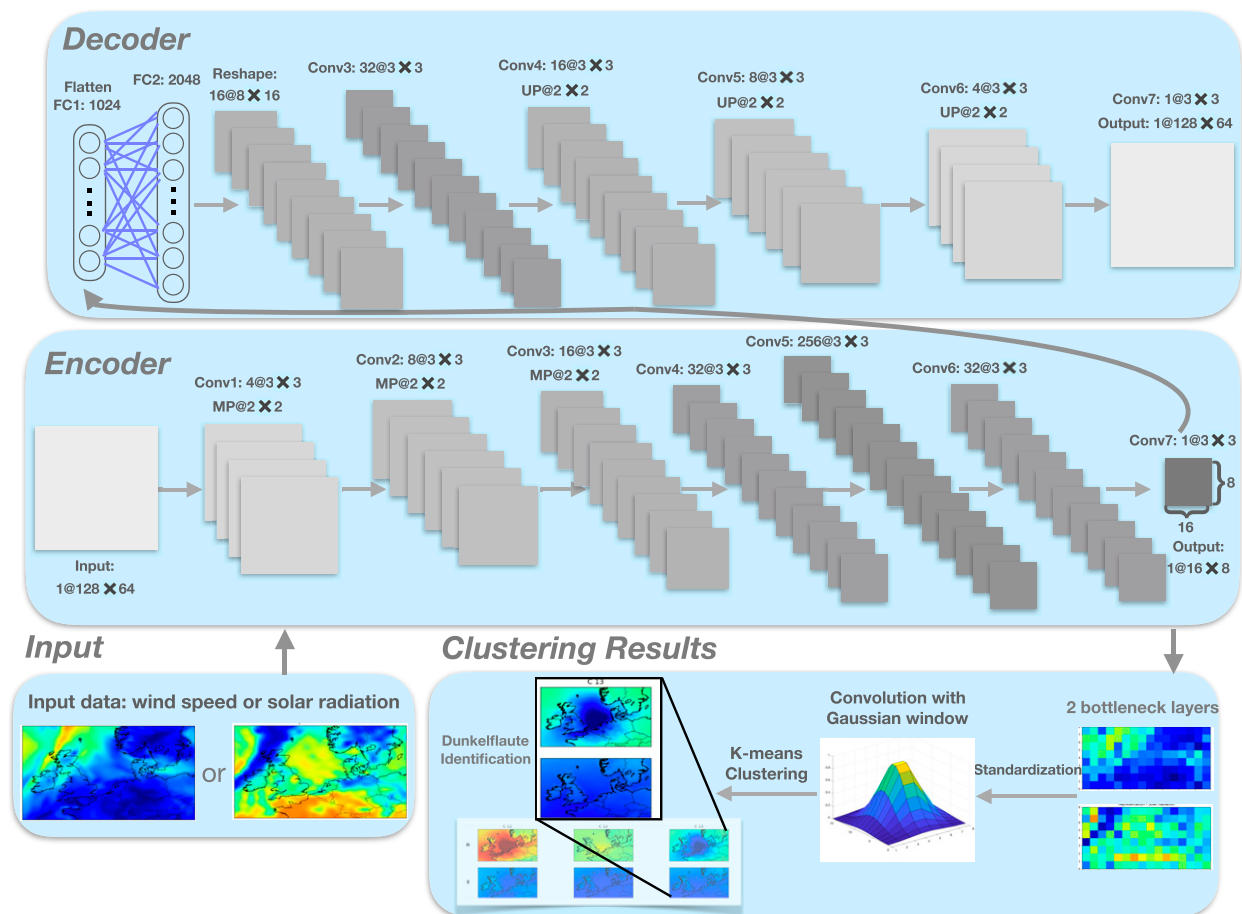


FIG. 2. Schematic of the proposed WISRnet framework.

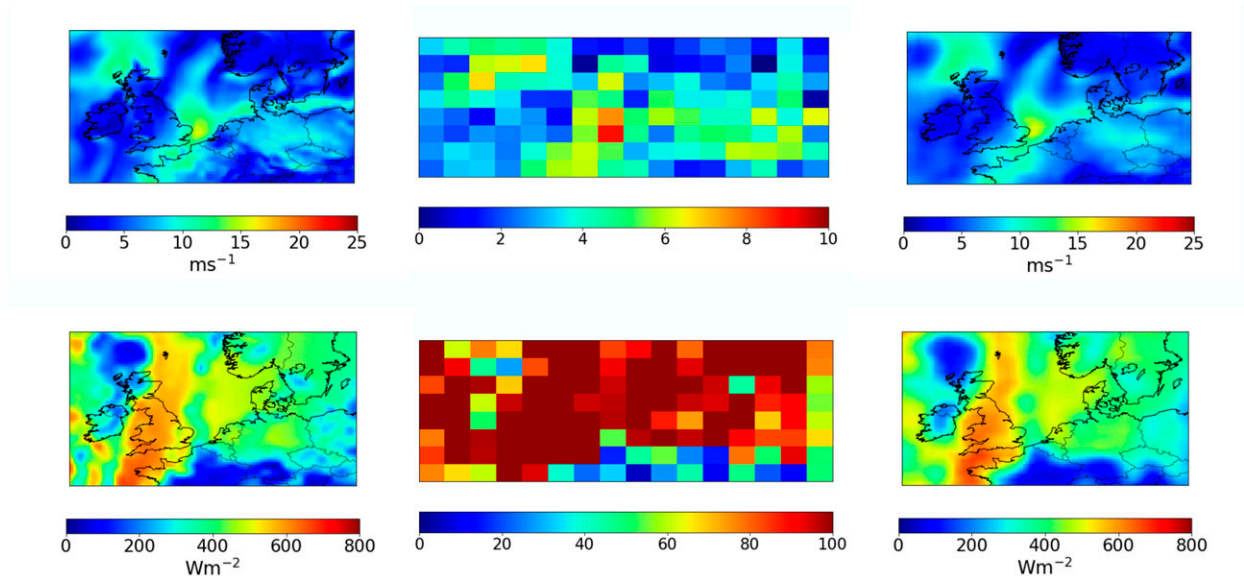


FIG. 3. An illustrative example from the validation dataset of the (left) original, (center) encoded, and (right) reconstructed maps of the (top) wind speed and (bottom) insolation fields from the CNN-AE. This is a randomly selected example (1600 UTC 14 May 2018), not a Dunkelflaute case.

data, we use an unsupervised method for the purpose of Dunkelflaute identification.

In the atmospheric science literature, several unsupervised clustering methods, including *k*-means, hierarchical clustering, and self-organizing maps, have been used for classification of synoptic weather patterns (Cheng and Wallace 1993; Fereday et al. 2008; Joseph et al. 2011; Bao and Wallace 2015; Sahai et al. 2017). In addition, they have been found useful in explaining trends in extreme temperatures (Horton et al. 2015) and facilitating weather forecasts (Ferranti et al. 2015; Neal et al. 2016; Totz et al. 2017). They are also popular for identifying extreme weather patterns (Grotjahn et al. 2016; Vigaud et al. 2018; Chattopadhyay et al. 2020a), wind power prediction (Dong et al. 2016; Wang et al. 2018), and other meteorological applications (Cassano et al. 2007; Johnson et al. 2008; Lee and Feldstein 2013).

In parallel to classical unsupervised ML approaches, in recent years, supervised convolutional neural networks (CNNs) have demonstrated their strengths in pattern classification. They have achieved excellent results in object detection and pattern recognition (Krizhevsky et al. 2012; LeCun et al. 2015). CNNs can automatically learn and extract representative features from multidimensional datasets, such as images and videos. They achieve high accuracy in classifying complex geophysical patterns, like clouds (Zhang et al. 2018), ice crystal (Xiao et al. 2019), land surface type (Li et al. 2014), and volcano deformation (Anantrasirichai et al. 2018). These examples show the benefits of supervised CNN. However, labeled datasets are often not available for various applications (e.g., Anantrasirichai et al. 2018; Chattopadhyay et al. 2020a). Thus, it is necessary to investigate the capability of CNNs implemented in an unsupervised manner. Recently, unsupervised CNNs have been used for classifying cloud

organizations (Denby 2020). In another application (Jiang et al. 2021), it has been utilized for creating flood inundation maps from synthetic aperture radar images.

Instead of unsupervised learning, a handful of recent studies exploited a new ML paradigm called self-supervised learning (Jing and Tian 2020; Kolesnikov et al. 2019). In this approach, the labels are automatically generated either by a separate pretrained model (e.g., Peng et al. 2020), or via common image transformations (e.g., Acuña-Escobar et al. 2022).

Clustering large datasets with high-dimensional feature vectors is a challenging task. The feature vectors may be nonlinear and/or nonstationary; for geophysical problems, they often exhibit multiscale behaviors. Various types of noise are also omnipresent. In some cases, the smaller scales may not be very relevant for the global characterizations. Under these circumstances, brute-force learning and clustering of the high-dimensional feature vectors may lead to overfitting and reduced generalization. To circumvent this problem, a type of unsupervised neural network, known as an autoencoder (AE; Hinton and Zemel 1994; Racah et al. 2017; Dong et al. 2018), can be first employed. Autoencoders do not require any labels as their sole objective is to extract important features from high-dimensional inputs. They map the inputs to outputs via encoding with minimal loss of information. In atmospheric science literature, a few studies have clustered weather patterns and extremes using CNN-based AE algorithms (Racah et al. 2016; Chattopadhyay et al. 2020a,b) and produced promising results. In this study, we develop a new CNN-AE architecture to automatically compress spatial wind speed and insolation patterns into low-dimensional encoded patterns. More technical information on an AE is provided in appendix A.

The encoded CNN-AE patterns are then clustered via the *k*-means algorithm. Since Dunkelflaute events are geographically

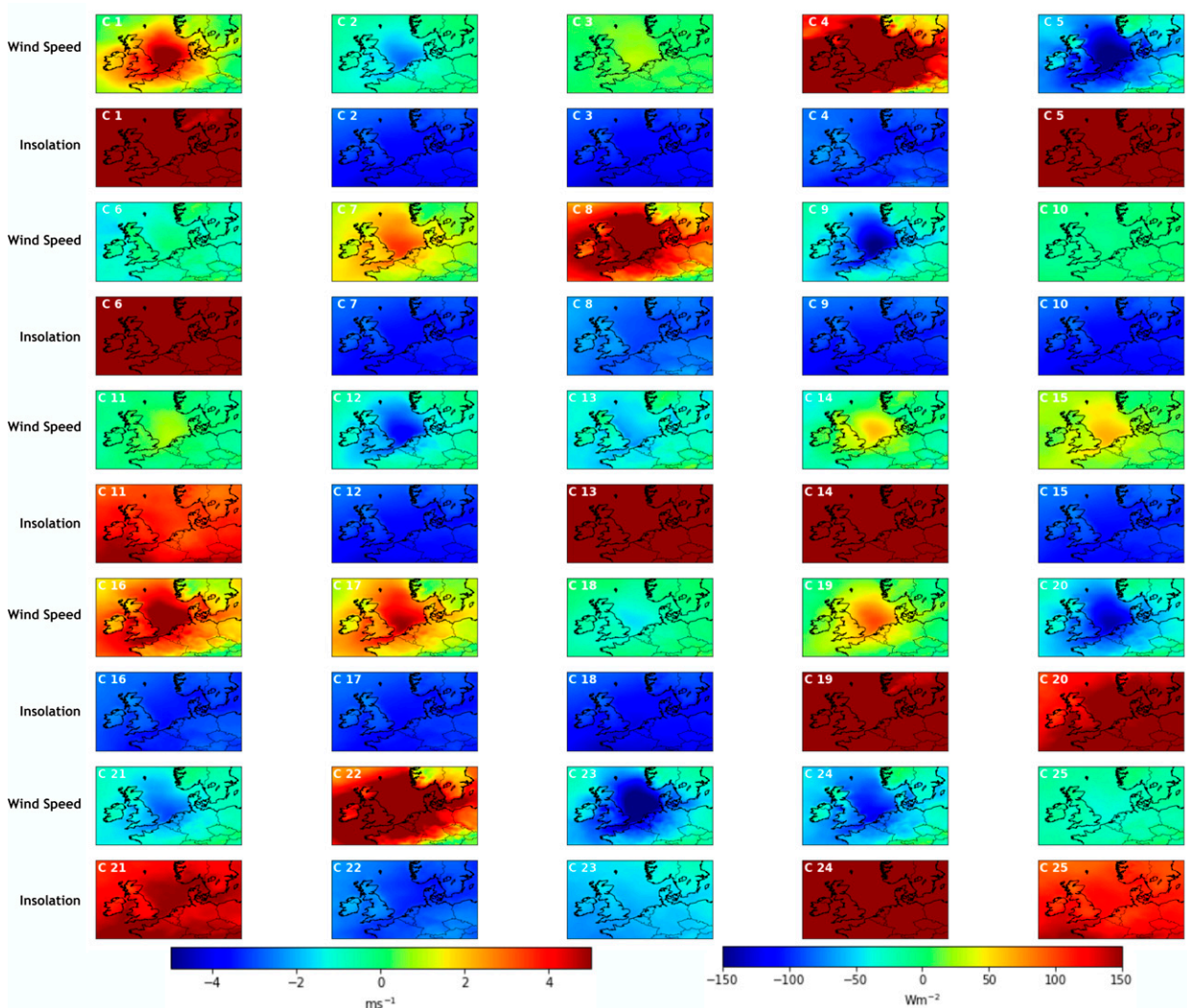


FIG. 4. Anomalies of wind speed and insolation based on the 10-yr mean for the 25 clusters (C1–C25) using the CNN-AE patterns. The Gaussian kernel is centered on Belgium.

localized phenomena, their clustering should account for spatial information. Thus, we make use of a geographically dependent k -means algorithm. In principle, more advanced clustering techniques (e.g., self-organizing maps) can be utilized instead of k -means; however, we opted for this well-known approach for its simplicity. Advantages and disadvantages of various clustering algorithms can be found in Grotjahn et al. (2016).

3. Description of datasets

The performance of deep learning models typically (with some exceptions) depends on the availability of high-quality training data. In situ wind speed and insolation data are often collected at sparse locations; the data records are usually short in duration and might suffer from temporal discontinuities. The measurements are also susceptible to terrain effects (e.g.,

shadowing) and measurement errors. To avoid these issues, in this proof-of-concept study, we use the ERA5 reanalysis dataset from the European Centre for Medium-Range Weather Forecasts (Hersbach et al. 2020). This global reanalysis has the highest temporal (hourly) and spatial resolution (~ 31 km) among its contemporaries. More importantly, in previous Dunkelflaute research (Li et al. 2021a,b), this dataset was shown to be very reliable for capturing numerous traits of Dunkelflaute events.

In this study, we use hourly wind speed data from 100 m above ground level (AGL) and downward shortwave radiation flux (insolation) at the surface. The time period of interest is from year 2009 to 2018. For both the variables, the sample size is 86 904. We concentrate our analysis over the North Sea and neighboring countries given the massive amount of ongoing and proposed wind farm installations in this region. Specifically, our domain of interest covers the region 46.75° – 62.5° N

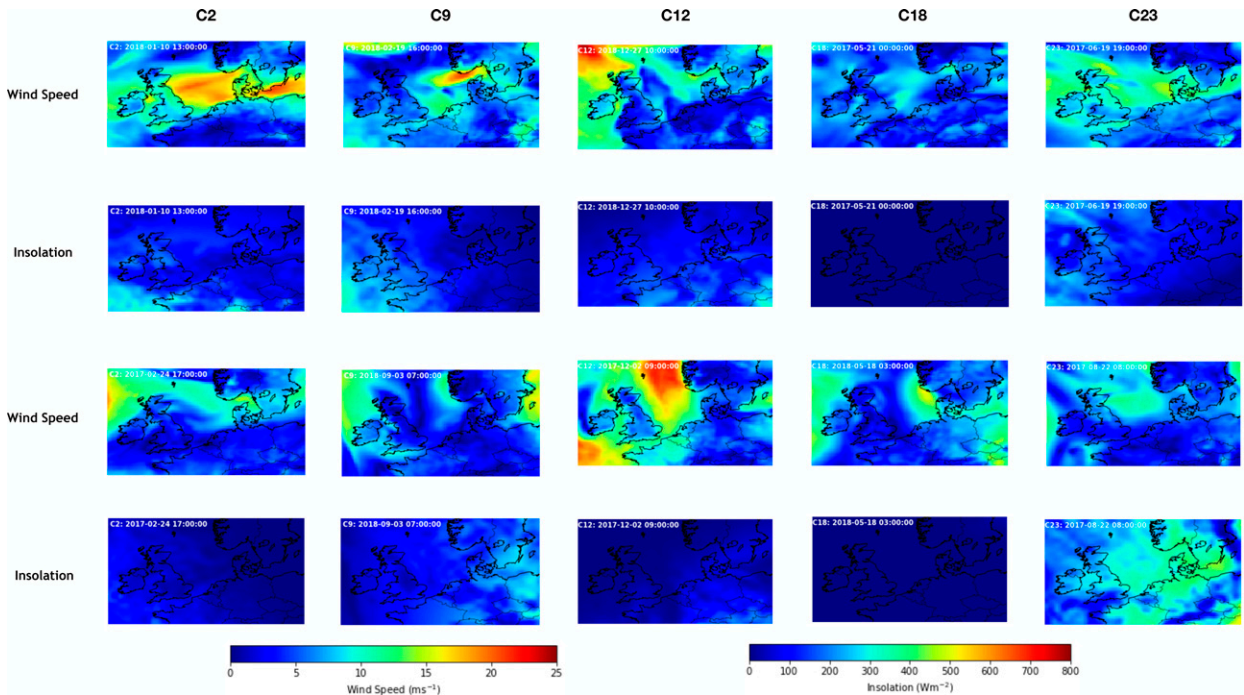


FIG. 5. Two randomly selected events for each of the top 5 clusters associated with periods of Dunkelflaute. Actual values (i.e., not anomalies) of wind speed and insolation are shown, and the clusters are based on the CNN-AE patterns with the Gaussian kernel centered on Belgium.

and 12°W – 19.75°E (consisting of 64×128 latitude–longitude grid points). An illustrative example of a Dunkelflaute event is shown in Fig. 1. This event occurred on 16 January 2017 over Belgium and caused a significant drop in renewable power generation (Truys and Vandervelden 2017).

For the validation of our proposed clustering framework, we use aggregated wind and solar power production data from Belgium. These datasets along with information on installed capacity were provided by the Belgian system operator Elia (<https://www.elia.be>). The selected validation period is from 2013 to 2018 since the aggregated power production data are only available from 2013. We aggregate the measured power data from a sampling rate of 15 min to 60 min be consistent with the hourly meteorological data from the ERA5 dataset. In Li et al. (2021a), a particular sample is tagged as a Dunkelflaute event if both wind and solar power production fall below the threshold of 20% of their respective capacities during that 60-min period. They reported that Dunkelflaute events lasting more than one day predominantly occur during the extended winter period (October–February). In the present work, for validation, we also use the same definition for labeling samples as Dunkelflaute or non-Dunkelflaute.

4. Methodology

a. Overview of the WISNet framework

The deep learning (DL) architecture used to cluster weather patterns and identify Dunkelflaute events is shown in Fig. 2. Henceforth, we refer to our framework as the

WISNet. For the training process, wind speed and insolation data are separately input into the CNN-AE model that “learns” weather patterns. The encoder part of the CNN-AE consists of seven convolutional layers that encode the input characteristics. The last layer of the encoder (i.e., the encoded pattern) is sometimes called a bottleneck layer. Commonly, a 1D fully connected (FC) layer is used as a bottleneck layer. However, 2D encoded patterns can be easily projected to the underlying geographical map and then convolved with a spatially varying weight matrix (e.g., a 2D Gaussian kernel). As a result, the 2D patterns are well suited to identify features with spatial relationships. For this reason, in this study, we use a 2D bottleneck layer.

In the literature, the decoder part of an AE is often just a mirror image of the encoder (Ranzato et al. 2007; Badrinarayanan et al. 2017). However, there are exceptions. For example, Chattopadhyay et al. (2020b) employed an asymmetric AE (named CapsNets) to predict the occurrence of cold and heat waves. Here, we use two FC layers and five convolutional layers in the decoder part to reconstruct input weather patterns. In contrast to the convolutional layers, the FC layers lose spatial information due to the flattening operation. However, their inclusion in the WISNet architecture is justified as they clearly improve the overall quality of the reconstructed fields (more information is provided in appendix B).

The accuracy of the CNN-AE model is assessed by comparing the input and the corresponding reconstructed patterns. Root-mean-squared error is used as a loss function.

TABLE 1. The correlation between periods of Dunkelflaute based on Belgian wind and solar power data and the clustered wind speed and insolation data between 2013 and 2018. The top 5 clusters in terms of DF time ratio are shown in bold.

Cluster	DF time ratio			Mean actual CF		Positive ratio			Number of samples
	>12 h	>24 h	All	Wind	Solar	>12 h	>24 h	All	
C1	0	0	0	0.6223	0.3070	0	0	0.0029	690
C2	0.1701	0.1630	0.1654	0.1293	0.0138	0.5969	0.1715	0.8110	3773
C3	0.0383	0.0517	0.0590	0.2929	0.0097	0.1405	0.0568	0.3026	3609
C4	0	0	0	0.7786	0.0344	0	0	0	237
C5	0.0030	0.0040	0.0025	0.0279	0.4732	0.0331	0.0132	0.0380	1209
C6	0.0016	0.0025	0.0018	0.2240	0.4413	0.0148	0.0070	0.0232	1420
C7	0.0047	0.0093	0.0081	0.4580	0.0177	0.0219	0.0128	0.0521	2880
C8	0	0	0	0.7245	0.0370	0	0	0	1526
C9	0.1727	0.1600	0.1378	0.0595	0.0146	0.8822	0.2452	0.9846	2590
C10	0.0751	0.0887	0.1017	0.2338	0.0126	0.2547	0.0903	0.4828	3898
C11	0.0100	0.0123	0.0152	0.2949	0.2068	0.0770	0.0286	0.1645	1714
C12	0.1958	0.1539	0.1726	0.0986	0.0141	0.7397	0.1744	0.9118	3503
C13	0.0026	0.0048	0.0028	0.1332	0.4684	0.0233	0.0127	0.0340	1499
C14	0.0003	0	0.0005	0.3510	0.4407	0.0046	0	0.0104	862
C15	0.0162	0.0245	0.0250	0.3741	0.0191	0.0645	0.0291	0.1393	3331
C16	0	0	0.0002	0.6418	0.0278	0	0	0.0020	2006
C17	0.0005	0.0017	0.0017	0.5503	0.0233	0.0026	0.0026	0.0115	2700
C18	0.1259	0.1411	0.1379	0.1800	0.0106	0.4180	0.1405	0.6405	3986
C19	0.0009	0.0012	0.0016	0.4637	0.2702	0.0102	0.0043	0.0247	1174
C20	0.0340	0.0322	0.0302	0.0592	0.2429	0.3189	0.0907	0.3955	1411
C21	0.0329	0.0315	0.0362	0.1053	0.2329	0.2469	0.0709	0.3808	1762
C22	0	0	0	0.7862	0.0316	0	0	0	987
C23	0.0857	0.0761	0.0641	0.0362	0.0521	0.8873	0.2363	0.9280	1278
C24	0.0022	0.0035	0.0020	0.0681	0.5155	0.0197	0.0095	0.0251	1472
C25	0.0275	0.0376	0.0335	0.1879	0.2108	0.1872	0.0768	0.3198	1939

The encoded patterns, resulting from respective wind speed and insolation inputs, are first normalized, and then, convolved with a 2D Gaussian kernel. The center of the Gaussian kernel is prescribed based on the country of interest. For example, the geophysical center of Belgium (latitude: 51.547°N and longitude: 4.610°E) is chosen as the kernel center, when we are identifying Dunkelflaute events in and around Belgium. Next, the convolved patterns are clustered using the k -means algorithm.

b. First step of the WISNet framework: Spatial pattern extraction

Wind speed and insolation values are inputted to the CNN-AE model in the form of a 64×128 longitude–latitude grid (see Fig. 1). Two CNN-AE models with different weights are trained for wind speed and insolation, respectively as depicted in Fig. 2. There are seven convolutional layers in the encoding part with 4, 8, 16, 32, 256, 32, and 1 filter, respectively. Each convolution filter has a kernel size of 3×3 and zero padding is applied to keep the size constant in each layer. All layers are followed by a rectified linear unit (ReLU) activation function to introduce nonlinearity to the CNN-AE model (Agostinelli et al. 2014). For the first three convolutional layers, max-pooling (MP) with a kernel size of 2×2 and stride of 1 is used to effectively halve the dimensions of the data to enhance learning efficiency, while the last four layers are connected directly without pooling layers. The CNN-AE outputs a two-dimensional encoded pattern (aka the bottleneck

layer) of dimensions 16×8 for both wind speed and insolation. Please refer to appendix B regarding the accuracy of the CNN-AE model.

As mentioned earlier, we use an asymmetric CNN-AE framework. In the decoding part, there are two FC layers with 1024 and 2048 neurons followed by four convolutional layers. The number of filters used in the convolutional layers is 32, 16, 8, 4, and 1, respectively; and there are three up-sampling layers between the layers to ultimately return to the input dimensions.

To evaluate the performance of the CNN-AE model, the ERA5 data are divided into three sets, where the first 80% of the samples are chosen for the training set, the following 10% of samples for the validation set, and the last 10% as the test set. The samples are contiguous in each set to avoid any information leakage across sets. The kernel filters are used for extracting characteristics, and they are updated using the back-propagation method. The adaptive moment estimation (Adam) is utilized as the optimizer (Kingma and Ba 2014). The maximum number of epochs is set to 100 with a batch size of 128, and the validation loss is estimated after each epoch. The hyperparameters, including kernel size, number of filters, number of convolutional layers, and learning rate are optimized in terms of the lowest validation loss and the highest accuracy in the reconstruction of the input fields. There is no visual evidence of overfitting in learning curves; furthermore, the application of dropout regularization did not improve the overall results. Please refer to appendix B for further details.

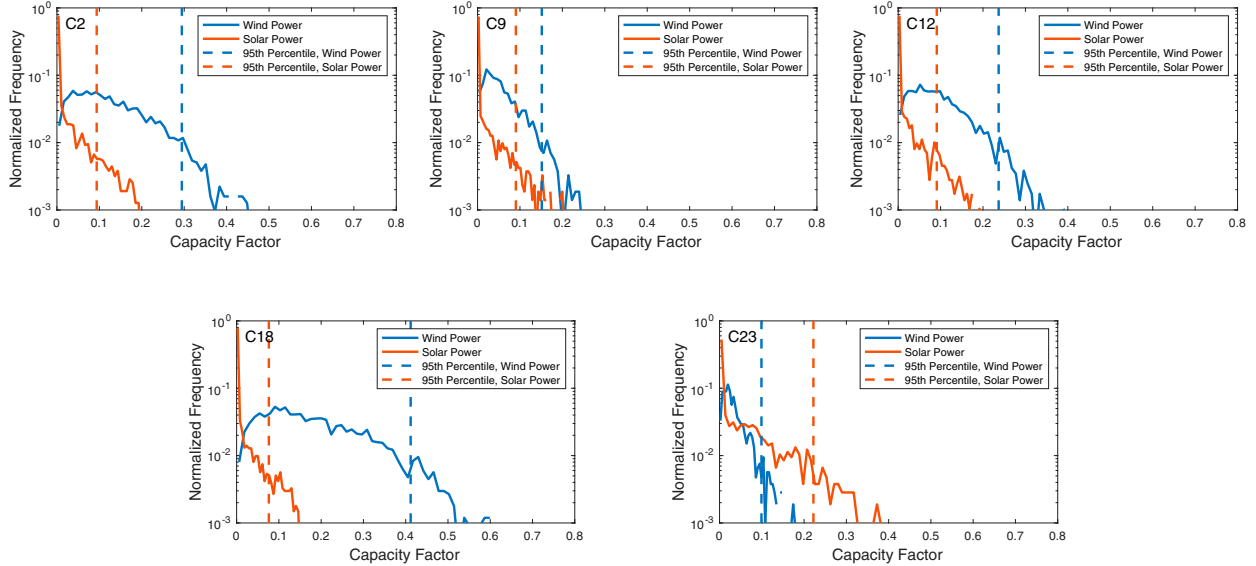


FIG. 6. Normalized frequency of capacity factor for the top 5 clusters associated with Dunkelflaute events. Aggregated power production data for the years 2013–18 (data source: <https://www.elia.be>) are used for the analysis. From top left to bottom right the clusters are C2, C9, C12, C18, and C23. Dashed lines represent the 95th percentile values for wind and solar power.

c. Second step of the WISRnet framework: Weather pattern clustering

In Li et al. (2021a), we reported that the correlation of Dunkelflaute occurrences in nearby areas decreases with increasing distance. Thus, we do not cluster the weather patterns for a specific country; rather, we use a spatially varying weight matrix for the entire domain of interest. First, the two encoded patterns (corresponding to wind speed and insolation fields) from the CNN-AE are standardized by subtracting the overall mean and normalized by overall standard deviations. Then, these normalized values are convolved with the following Gaussian kernel:

$$f(x, y) = \frac{1}{2\pi\sigma_x\sigma_y} \exp\left\{-\left[\frac{(x - \mu_x)^2}{2\sigma_x^2} + \frac{(y - \mu_y)^2}{2\sigma_y^2}\right]\right\}, \quad (1)$$

where μ_x and μ_y are the coordinates of the geographical center of interest. The variables σ_x and σ_y are related to region of influence in the x (longitudinal) and y (latitudinal) directions, respectively. Their prescribed values depend on the size of the country of interest. For an area the size of Belgium, a value of 1 was used for both σ_x and σ_y .

The k -means algorithm (Lloyd 1982) is used to cluster the convolved CNN-AE patterns into 25 weather clusters. As discussed in appendix C, we have found that 25 clusters are appropriate for the convergence of k -means clustering and identifying the most characteristic features of wind speed and insolation patterns.

Before discussing the results, we would like to emphasize that our region-dependent clustering technique is important for reducing the total number of clusters. Without this technique, the difference between Dunkelflaute in different

countries will be difficult to distinguish with only 25 clusters; please refer to appendix D for more details.

In appendix E, we use self-organizing map (SOM) as a baseline to cluster weather patterns and compare its results with the proposed WISRnet framework.

5. Results

a. Feature extraction

Figure 3 shows an illustrative example from the validation set of an original (left), encoded (middle), and reconstructed (right) map of the wind speed and insolation fields. The encoded maps can be seen to capture the main features of wind speed and insolation maps, for example, higher encoded values corresponding to higher wind speed or insolation. In addition, the CNN-AE patterns have similar spatial distributions as the original ones, which means that the location information is not lost. The reconstructed map is used to evaluate the performance of the CNN-AE. As seen in the illustrative example in Fig. 3, the original wind speed and insolation field are reproduced well. For the entire validation set, the root-mean-squared errors between the original and the reconstructed values are 0.78 m s^{-1} and 24.62 W m^{-2} for the wind speed and insolation, respectively. Since the wind speed and solar radiation in the whole dataset can go up to about 44.57 m s^{-1} and 1010.85 W m^{-2} with the average of 7.77 m s^{-1} and 123.46 W m^{-2} , respectively, the errors are moderately low.

b. Weather pattern clustering

In Fig. 4, we show the clustering results of the CNN-AE patterns with the Gaussian weighting kernel centered on

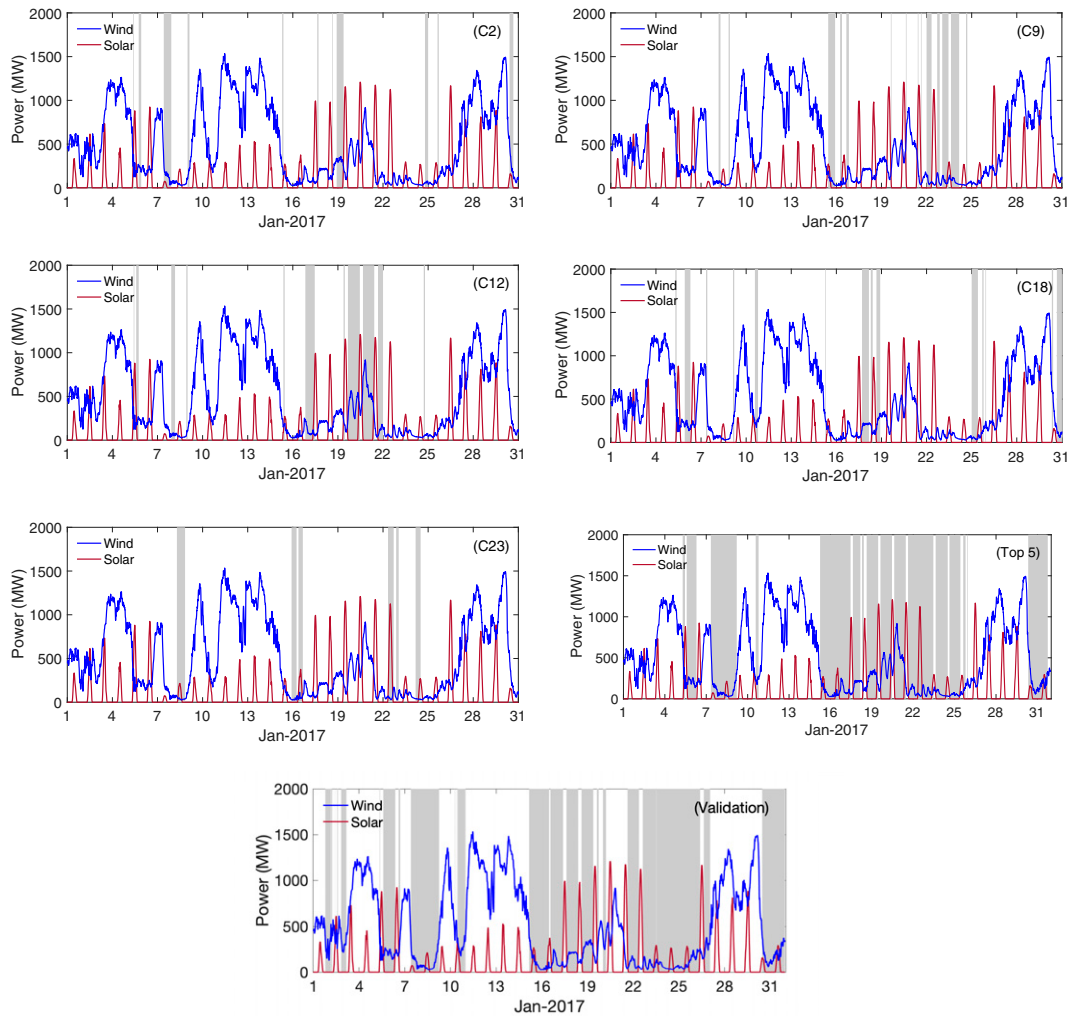


FIG. 7. Time series of wind and solar energy production during January 2017 (data source: <https://www.elia.be>). In the top six panels, the shaded gray regions represent the Dunkelflaute periods identified by the C2, C9, C12, C18, and C23 clusters, respectively, and all these periods combined (marked “top 5”). In the bottom panel, the Dunkelflaute time is demarcated by a gray shade if both wind and solar power production fall below the threshold of 20% of their respective capacities using Elia data. This plot is used for validation.

Belgium. For each of the 25 clusters, mean wind speed and insolation anomalies are calculated based on the 10-yr mean values for all clusters. Different clusters exhibit different magnitudes and extent of wind speed and insolation with a clear focus over Belgium. From visual inspection, the clusters C2, C9, C12, C18, and C23 are most closely related to periods of simultaneous low wind speed and insolation over Belgium. These clusters (herein “top 5” clusters) seem to be the most suitable candidates for identifying cases of Dunkelflaute and will be analyzed in the next section.

To illustrate how well the clusters capture the characteristics of individual events, in Fig. 5, we show two randomly selected events for each of the top 5 clusters associated with periods of Dunkelflaute. Actual values of wind speed and insolation are shown. For all 10 events, low wind speeds and low levels of insolation are apparent over Belgium.

c. Identification and verification

In Table 1, we examine how frequently Dunkelflaute events actually occur for each cluster and what fraction of events are Dunkelflaute events in each cluster based on actual Belgian wind and solar power generation data for the period 2013–18. We classify a particular event as a Dunkelflaute event if both wind and solar power production fall below the threshold of 20% of their respective capacities (Li et al. 2021a). Dunkelflaute periods are then matched to the appropriate cluster for that period. In the table, the Dunkelflaute (DF) time ratio is calculated as the ratio of Dunkelflaute events in each cluster to the total number of Dunkelflaute events. The events lasting longer than 12 or 24 h are labeled as “>12 h” and “>24 h,” respectively. The label “All” is used in Table 1 to denote all events. The top 5 clusters in terms of DF time ratio are shown in bold. We would like to emphasize that these same

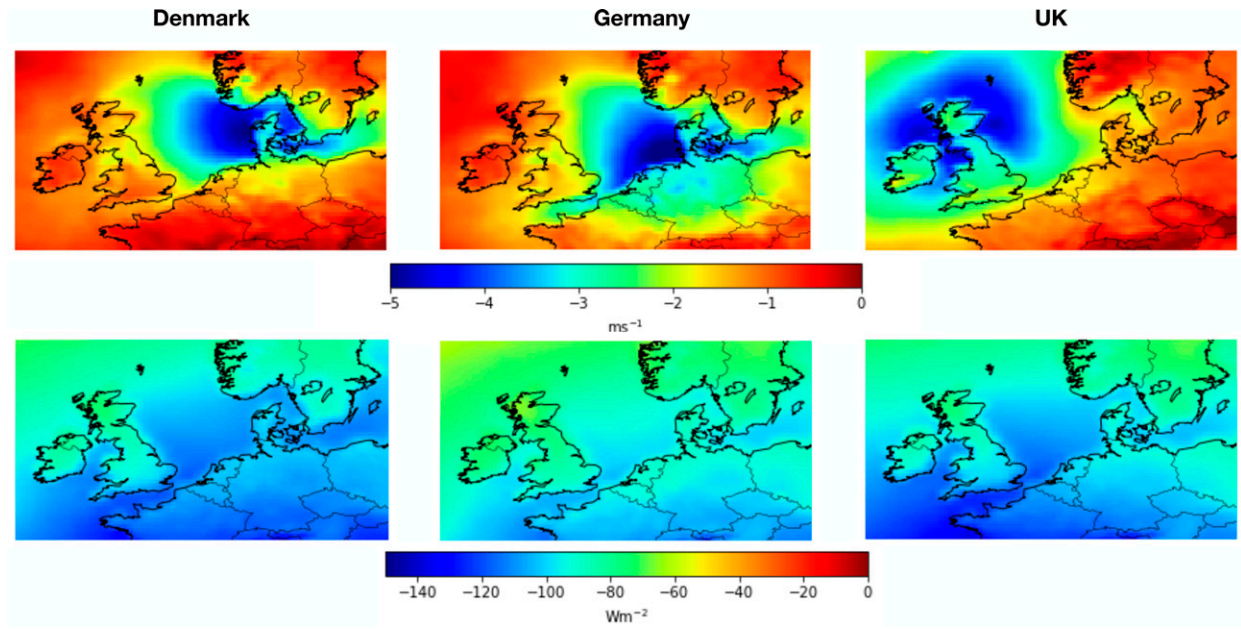


FIG. 8. Anomalies of (top) wind speed and (bottom) insolation for weather patterns clustered as Dunkelflaute centered over (left) Denmark, (center) Germany, and (right) the United Kingdom.

five clusters were visually identified earlier as suitable candidates for identifying Dunkelflaute events. These five clusters account for 75% of all Dunkelflaute events greater than 12 h, 69% of all such events greater than 24 h, and 68% for all the events.

The mean wind and solar power capacity factors (CF) for each of the 25 clusters are also listed in Table 1. The capacity factor is defined as the fraction of wind and solar power production normalized by their respective installed capacities. For the C9, C12, and C23 clusters, the mean capacity factors are especially low, with values less than 10% for both wind and solar power. The mean solar power capacity factors for the C2 and C18 clusters are equally low, while wind power capacity factors for them are slightly higher.

To further illustrate the correlation of Dunkelflaute events to specific clusters, the fraction of Dunkelflaute events as a ratio of total events in each cluster, named “positive ratio,” is shown in Table 1. This ratio is simply calculated by dividing the number of hourly Dunkelflaute samples by the total number of samples in a specific cluster. It can be seen that over 90% of the events in clusters C9, C12, and C23 are Dunkelflaute events. This would suggest that these clusters are a reliable indicator of whether an event is a Dunkelflaute event. Clusters C2 and C18 are a less reliable indicator but nonetheless indicate a high probability of an event being a Dunkelflaute event. Some level of incorrect clustering can be explained by overestimation of the magnitude of insolation in the ERA5 reanalysis (Babar et al. 2019; Sianturi et al. 2020), especially for the cloudy days that are of interest for this work.

The top 5 clusters all have mean capacity factors lower than 20%, which is exactly the threshold for defining Dunkelflaute.

Thus, associating these clusters to Dunkelflaute events is rather straightforward. However, for three other clusters (C10, C20, and C21), such an inference cannot be drawn in a conclusive manner. These clusters have mean capacity factors marginally higher than the threshold of 20%. They also include a handful of Dunkelflaute events. Specifically, for Dunkelflaute events longer than 12 h, the clusters C10, C20, and C21 have DF time ratios of 8%, 3%, and 3%, respectively. At the same time, they have positive ratio of only 25%, 32%, and 25%, respectively. Thus, if these clusters are identified as Dunkelflaute clusters, there will be a large number of false positive samples. In this study, we favored missing out on a few events instead of including too many non-Dunkelflaute events in our analysis.

Figure 6 shows the frequency of the capacity factors for the top 5 Dunkelflaute clusters, as well as the plots for the 95th percentile values for wind and solar power. It is clear that approximately 95% of the samples clustered in the C9, C12, and C23 clusters have capacity factors lower than 25%. While for the C2 and C18 clusters, most values lie within about 40% capacities, confirming these clusters as less reliable indicators of Dunkelflaute events. Besides, as shown in Table 1, the mean wind power capacity factors for four out of these five Dunkelflaute clusters are larger than the mean solar power capacity factors, resulting in the relatively smaller values for the 95th percentile for insolation.

Taking an actual Dunkelflaute case as an example, Fig. 7 shows the aggregated wind and solar power production data for January 2017 (Li et al. 2021b). Belgium experienced a total of nine days of Dunkelflaute in January 2017, during which flexibility options including more electricity generation from natural gas and additional power imports from neighboring countries were taken to circumvent the situation.

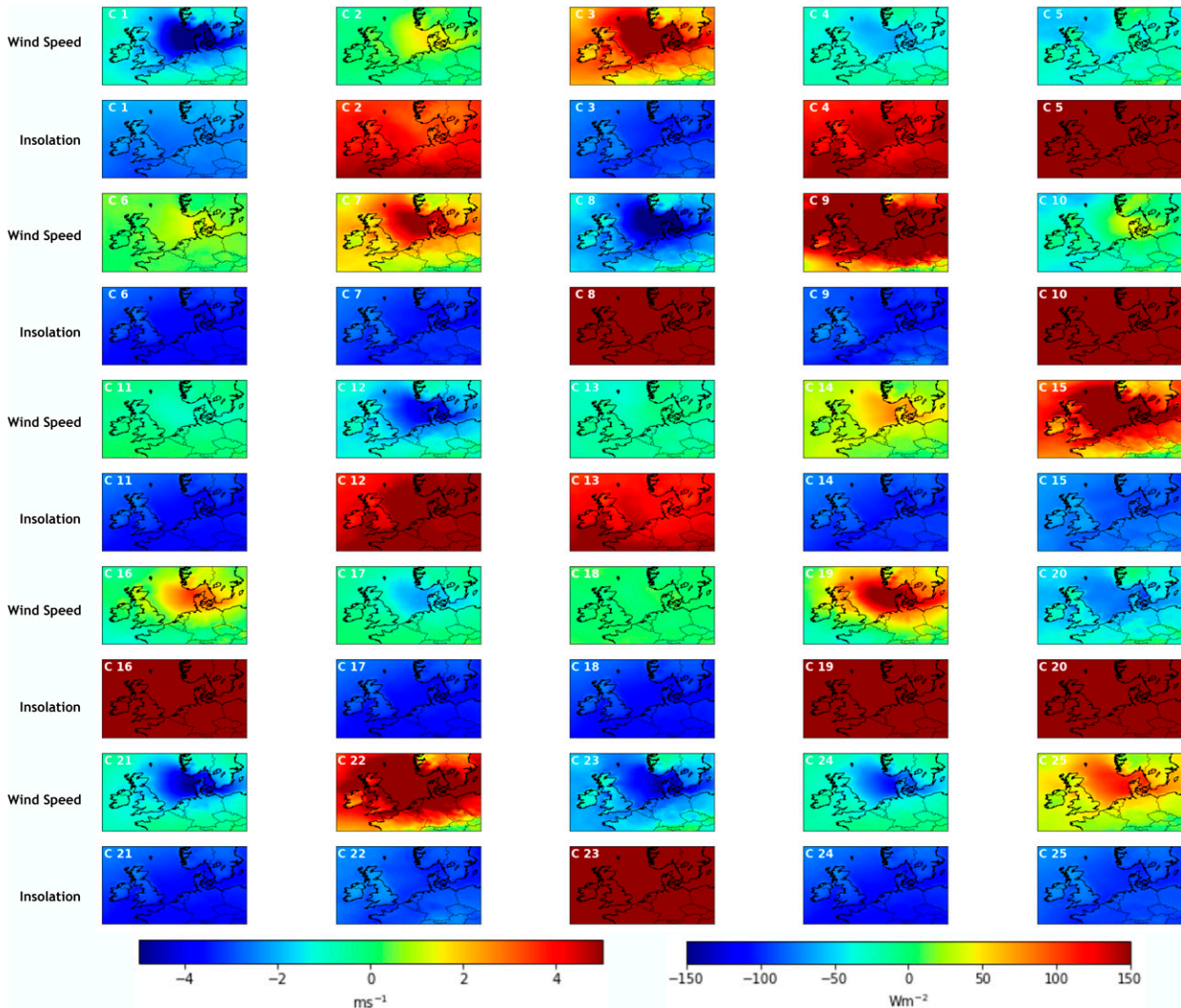


FIG. 9. As in Fig. 4, but the clustering algorithm is centered over Denmark.

The Dunkelflaute periods clustered in the individual five clusters identified previously (C2, C9, C12, C18, and C23) and all these five clusters together (marked “top 5”) are marked as shaded gray regions in the top six panels of Fig. 7. High correlation is seen between the Dunkelflaute periods based on actual power data (bottom panel of Fig. 7) and the clustered wind speed and insolation data in top 5 clusters. Each of the top 5 clusters identified some segments of the Dunkelflaute event.

d. Identification of Dunkelflaute for other European countries

The proposed WISRnet framework can also be applied to other countries to identify Dunkelflaute periods. Here, we utilize the framework for three additional countries: Denmark, Germany, and the United Kingdom. Anomalies of wind speed and insolation for the most representative clusters identified as Dunkelflaute are shown in Fig. 8 for each of the three

countries. Areas of anomalously low wind speed and insolation are clearly shown centered on the three countries of interest.

Taking Denmark as an example, the mean wind speed and insolation anomalies for 25 clusters are shown in Fig. 9. The clustered patterns clearly focus on Denmark and several clusters are characteristic of Dunkelflaute periods, i.e., C1, C21, and C24. For these three clusters, low wind speeds and insolation are present over Denmark and surrounding areas, covering a considerable part of the North Sea. It is also clear that negative anomalies of insolation extend over almost the entire domain.

6. Concluding remarks

This paper is the first to demonstrate the capability of a machine learning-based framework (named WISRnet) for identifying Dunkelflaute events using public-domain wind speed

and insolation data (e.g., reanalysis datasets). The crucial elements of the WISRnet are the CNN-AE architecture to extract the two-dimensional features from gridded weather data and the region-dependent k -means clustering. The combination of these elements enables the WISRnet to identify location-specific Dunkelflaute patterns. High accuracy is achieved when extracting encoded spatial patterns. Most importantly, excellent correspondence is seen between observed Dunkelflaute periods and those tagged as such using the WISRnet approach. Even though most of the present study has been focused on Belgium, the applicability of the WISRnet for other countries has also been briefly illustrated.

We believe that the clustering of Dunkelflaute events can be improved by including other types of meteorological data (e.g., satellite observations). In addition to wind speed and insolation, several other variables (e.g., mean sea level pressure, cloud-base height, low cloud cover) are closely related to Dunkelflaute events (Li et al. 2021a). The inclusion of some of these variables might also enhance the overall performance of the WISRnet. Furthermore, other clustering methods (e.g., SOM) and other spatial weighting algorithms may be more effective than our current approach. We hope to experiment with some of these alternatives in our future work.

The WISRnet framework, with minor adjustments, can be used in conjunction with various climate projection datasets (e.g., CMIP5). By doing so, one will be able to quantify the impacts of climate change on the characteristics of the Dunkelflaute events. It is needless to say that any statistically significant trend in the Dunkelflaute events will be of critical importance for the designing and planning of next-generation power systems.

Acknowledgments. The first author is thankful to the Chinese Scholarship Council for sponsoring her Ph.D. research.

Data availability statement. Aggregated power production and installed capacity data are available from the Belgian system operator Elia (<https://www.elia.be>). The ERA5 reanalysis data are provided by the European Centre for Medium-Range Weather Forecasts (<https://cds.climate.copernicus.eu>).

APPENDIX A

Autoencoder

An autoencoder comprises of an encoder part and a decoder part. The encoding process transforms the input patterns to the bottleneck layer with compressed amplitude and spatial information. For a given input dataset $\mathbf{x} \in \mathbf{R}^d$, a hidden layer in the encoder can be written as follows:

$$\mathbf{z} = f(\mathbf{x}) = \phi(\mathbf{W}_e \mathbf{x} + \mathbf{b}_1). \quad (\text{A1})$$

Here an encoder $f(\cdot)$ uses the activation function $\phi(\cdot)$ to introduce the nonlinearity. The terms $\mathbf{z} \in \mathbf{R}^s$, $\mathbf{W}_e \in \mathbf{R}^{s \times d}$,

and $\mathbf{b}_1 \in \mathbf{R}^s$ are the weight matrix and bias value given to the input features, respectively. Here d and s refer to the size of inputted and encoded patterns, respectively.

Then the decoder recreates the input patterns by mapping the encoded patterns back to the input features as follows:

$$\mathbf{y} = g(\mathbf{z}) = \phi(\mathbf{W}_d \mathbf{z} + \mathbf{b}_2), \quad (\text{A2})$$

where $g(\mathbf{z})$ indicates the mapping process between the hidden layer and the outputted features, and $\phi(\cdot)$ denotes the decoding activation function. Here, $\mathbf{W}_d \in \mathbf{R}^{d \times s}$ and $\mathbf{b}_2 \in \mathbf{R}^d$ represents the weight matrix and bias term of the decoder. The reconstruction uses trainable parameters $\theta = \{\mathbf{W}_e, \mathbf{W}_d, \mathbf{b}_1, \mathbf{b}_2\}$. The goal of the autoencoder is to output the features \mathbf{y} to be close to the input information \mathbf{x} to the maximum extent. It can be achieved through training by minimizing a loss function:

$$\mathbf{J}(\theta) = \sum_{\mathbf{x}} L(\mathbf{x}, \mathbf{y}) = \sum_{\mathbf{x}} L\{\mathbf{x}, g[f(\mathbf{x})]\}, \quad (\text{A3})$$

where L represents the loss function that is used to measure the reconstruction error. A regularization term can also be added to avoid overfitting. The minimization of the error term is usually implemented by stochastic gradient descent.

APPENDIX B

CNN

The CNN used here is developed using the TensorFlow-Keras library (Abadi et al. 2016; Gulli and Pal 2017). We have trained a number of CNNs including the symmetric architecture and asymmetric architecture of autoencoder, and several representatives are listed in the Table B1. The best symmetric algorithms we trained, named CNN3-FC1, has three convolutional layers with 8, 16, and 32 filters, respectively. The final feature map is flattened first and then connected to a dense layer that fully connected with 128 neurons. Regarding the asymmetric autoencoder algorithm, three representative structures, called Asym-CNN5, Asym-CNN7, and Asym-CNN10, use 5, 7, and 10 convolutional layers in the encoding part, respectively. The convolutional layers of Asym-CNN5 and Asym-CNN10 have 4, 8, 256, 32, and 1 filters and 4, 8, 16, 32, 64, 128, 256, 256, 32, and 1 filters, respectively. The Asym-CNN7 architecture is depicted in Fig. 2. For these four CNNs, all the filters in the convolutional layers have a kernel size of 3×3 and the first three convolutional layers are all followed by a ReLU activation function and a max-pooling layer. The max-pooling layer uses a kernel size of 2×2 and a stride of 1. For the decoding part, CNN3-FC1 is the reverse structure of its encoder. The decoder structures for the other three have the same number of layers as their encoding counterpart, specifically, two fully connected layers and 3, 5, and 8 convolutional layers, respectively.

TABLE B1. The RMSE between the input and the reconstructed patterns for nine different CNN-AE architectures. The bold font shows the best result.

RMSE	Learning rate	Dropout	FC layer	Wind speed (m s^{-1})			Insolation (W m^{-2})		
			First layer	Train	Validation	Test	Train	Validation	Test
CNN3-FC1	0.001	—	1024	0.76	0.76	0.80	24.85	33.50	26.59
Asym-CNN5	0.001	—	1024	0.80	0.81	0.85	22.12	25.45	24.27
Asym-CNN7	0.0005	—	1024	0.78	0.78	0.82	21.09	24.88	23.40
Asym-CNN7	0.001	—	1024	0.78	0.78	0.81	21.26	24.62	23.06
Asym-CNN7	0.005	—	1024	4.47	4.48	4.52	193.74	191.82	200.13
Asym-CNN7	0.001	0.5	1024	1.36	3.42	3.39	39.26	109.59	113
Asym-CNN7	0.001	0.25	1024	1.13	1.95	1.96	30.31	61.82	62.76
Asym-CNN7	0.001	—	128	0.98	0.97	1.02	26.03	28.22	26.97
Asym-CNN10	0.001	—	1024	4.47	4.49	4.52	23.16	25.83	29.12

The RMSE between the input and the reconstructed wind speed and insolation patterns for training, validation and test sets for selected runs are listed in Table B1. Though the results of CNN3-FC1 is competitive, the application of symmetric architecture leads to a 1D encoder and is not suitable for the 2D clustering algorithm. We also investigated the influence of other hyperparameters like the number of convolutional layers (from 2 to 10), the number of filters (e.g., 4, 8, and 16 filters for the first convolutional layer), and the kernel size (from 3×3 to 7×7) of convolutional filters on the overall performance. It is found that the performance of an algorithm with less than 7 convolutional layers is not as satisfactory while using more than 7 convolutional layers can overfit the results. Overall, the best accuracy is from Asym-CNN7 (refer to Table B1).

The maximum number of epochs is set to 100 with a batch size of 128, and the accuracy performance is estimated after each epoch. The learning curves are shown in the two panels of Fig. B1, which illustrated the change of loss with epochs for wind speed and insolation patterns using Asym-CNN7. It is found that after 60 epochs, the decrease of RMSE of wind speed and insolation patterns tends to be relatively negligible for validation sets.

A few sensitivity runs are performed with the Asym-CNN7 architecture to quantify the impacts of (i) learning rate, (ii) dropout, and (iii) number of neurons in the FC layers. The best result with Asym-CNN7 is achieved with a learning rate of 0.001. For a larger learning rate (e.g., 0.005), the RMSE increases dramatically, while for a smaller learning rate (e.g., 0.0005), there is no further improvement in performance. To investigate the influence of regularization, a dropout rate of 0.5 and 0.25 is added to the FC layers sequentially. With increasing dropout rates, the RMSE values increase. Thus, dropout is not deemed to be an effective regularization strategy for this particular problem. To quantify the importance of the FC layers, an additional sensitivity run was performed. In this run, the number of neurons in the two FC layers are decreased to 128 and 256, respectively. In contrast, in the default case, these FC layers have 1024 and 2048 neurons, respectively. It is evident from Table B1 that the RMSE of reconstruction increases considerably with the reduction of the neurons in the FC

layers. In other words, the FC layers with sufficient complexity are needed to recreate the wind speed and insolation patterns accurately.

APPENDIX C

K-Means Clustering

A clustering approach groups all the objects into some subsets of similar wind speed and insolation patterns. The k -means clustering algorithm is widely used for its capability in clustering a great number of objects. It employs the squared error criterion of similarity that turns out to work well with a diversity of clusters (Jain et al. 1999). The squared error function in a cluster is calculated as the sum of squares of the distance between the patterns in each cluster and the cluster center as follows:

$$e^2 = \sum_{j=1}^K \sum_{i=1}^{n_j} \|\mathbf{x}_{i,j} - \mathbf{c}_j\|^2, \quad (\text{C1})$$

where $\mathbf{x}_{i,j}$ is the i th sample in the j th cluster. There are K clusters in total and each cluster has a centroid, for example, \mathbf{c}_j for the j th cluster.

The clustering begins with a random partition and then assigns the samples to the closest cluster centroid by measuring the data similarity and distance between the samples and the cluster centers. Here the centroid is the mean value of the patterns in each cluster. Subsequently, the cluster centers are recomputed, and the reassignment continues until there is no additional reduction of squared point-to-centroid distance after several iterations.

The number of clusters K is specified a priori and will influence the performance of the criterion function. In this study, we use two competing approaches to estimate the optimal value of K .

First, we calculate inertia (Pedregosa et al. 2011) to denote how well the data are clustered by k -means by summing the squared distances of samples to their closest cluster center. In the left panel of Fig. C1, it can be seen that the K value of 20–30 is optimal with low inertia, and there is little improvement of squared distance when the number of clusters is larger than 30.

Next, the Davies–Bouldin index is used (Davies and Bouldin 1979); refer to the right panel of Fig. C1. This index is defined

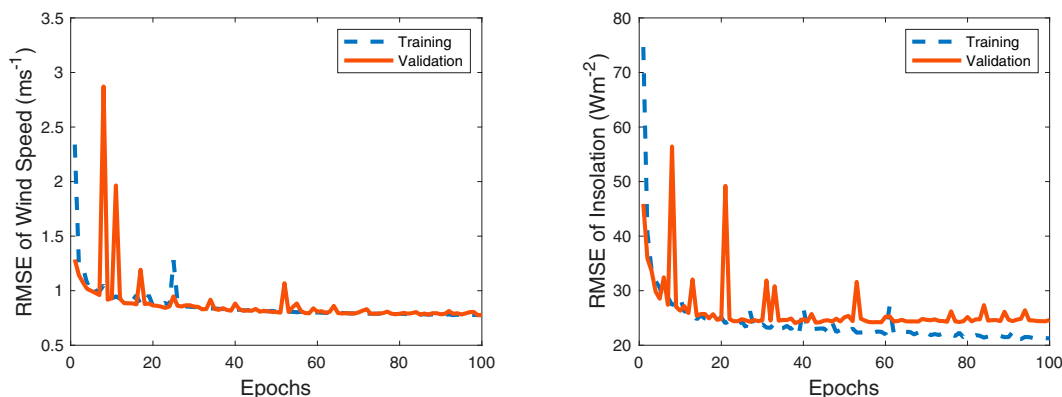


FIG. B1. Examples of learning curves for (left) wind speed and (right) insolation patterns. Loss is measured as RMSE between the input and the reconstructed wind speed and insolation patterns.

as the average similarity of each cluster with the cluster most similar to it. Thus, the smaller magnitude of the index means that clusters are better separated, leading to better clustering. According to Fig. C1 (right panel), the Davies–Bouldin index fluctuates somewhat erratically. There is a minimum corresponding to 2 clusters. For higher number of clusters, there is a general decreasing trend. However, it is not possible to estimate an optimal value of K from this plot. Hence, based on the inertia calculations, we opt for $K = 25$.

APPENDIX D

K-Means Clustering without Using a Gaussian Kernel

The region-dependent clustering technique aims to cluster weather patterns with a focus on a region or country of interest. A Gaussian kernel is used for convolution. To quantify the importance of this kernel, we document additional K -means clustering results in Fig. D1. In this computation, we do not use a Gaussian kernel. This figure should be compared against Fig. 4 where a Gaussian kernel is utilized. According to Fig. D1, it is clear that several clusters (e.g., C3, C6, C21) represent simultaneous low wind speed

and low insolation conditions. However, the spatial patterns are rather diffused instead of focused on a specific country.

APPENDIX E

Self-Organizing Map

SOM is a popular unsupervised machine learning approach and was originally developed by Kohonen (Kohonen 1990, 2013). A SOM can extract nonlinear patterns from data, and as such, is more powerful than commonly used linear approaches (e.g., principal component analysis, empirical orthogonal functions). The SOM-based classifications have been widely used in the atmospheric science field (Horton et al. 2015; Francis and Skific 2015; Ohba et al. 2016; Gibson et al. 2017; Loikith et al. 2017; Cheneka et al. 2021). In this appendix, we use SOM as a baseline to cluster wind speed and insolation patterns and compare its results with the WISRnet framework.

Before training a SOM network, wind speed and insolation data are first normalized and then concatenated together. The MiniSom package (Vettigli 2018), is employed here with a 5×5 SOM grid. The total number of nodes in this grid determines the number of resulting clusters. Since

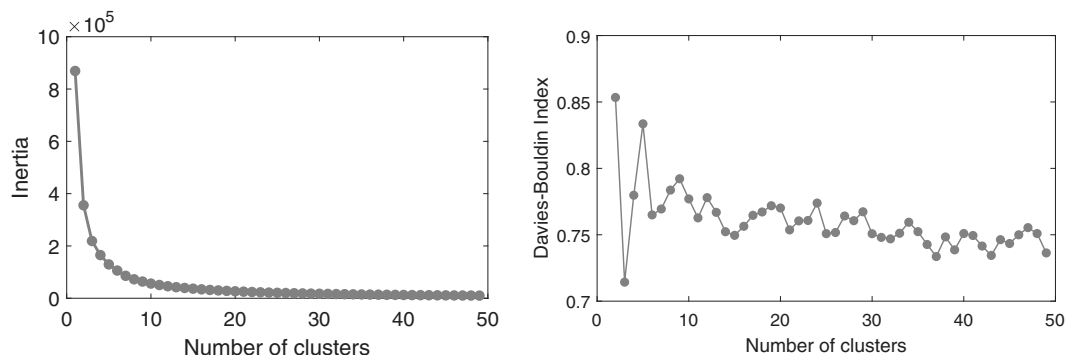


FIG. C1. The (left) change of inertia and (right) Davies–Bouldin index vary as a function of the number of clusters.

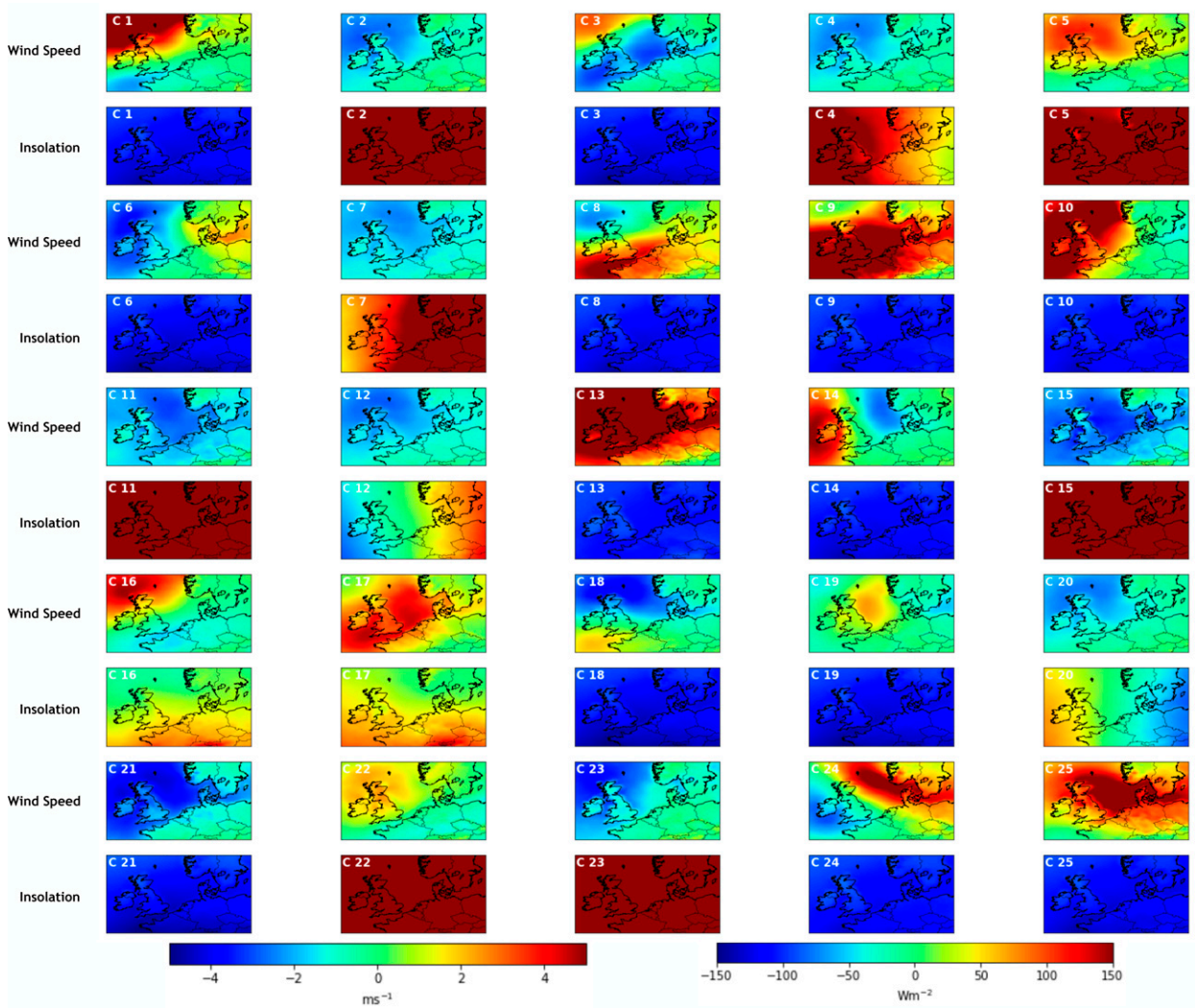


FIG. D1. Anomalies of wind speed and insolation based on the 10-yr mean for the 25 clusters (C1–C25) using the CNN-AE patterns. The Gaussian kernel is not included in the clustering technique.

our WISRnet framework uses 25 clusters, we use the same number of clusters with SOM. The learning rate of 0.01, neighborhood size of 1, and a high number of iterations of 1 000 000 are used in SOM implementation.

In Table E1, we examine the fraction of Dunkelflaute events as a ratio of total events in each cluster (positive

ratio) based on actual Belgian wind and solar power generation data for the period 2013–18. The top 5 clusters (S1, S11, S16, S17, and S21) in terms of positive ratio are shown in bold. It can be seen that approximately 70% of the events in clusters S1, S11, and S16 are Dunkelflaute events and there is a positive ratio of around 65% for S17 and S21.

TABLE E1. The positive ratio in each cluster based on Belgian wind and solar power data and the clustered wind speed and insolation data using SOM between 2013 and 2018. Here we include all events regardless of the duration. The top 5 clusters in terms of positive ratio are shown in bold.

Cluster	S1	S2	S3	S4	S5	S6	S7	S8	S9
Positive ratio	0.7112	0.3125	0.3556	0.0063	0.0017	0.3195	0.0620	0.2352	0.1551
Cluster	S10	S11	S12	S13	S14	S15	S16	S17	S18
Positive ratio	0.0840	0.7868	0.5177	0.5013	0.1134	0.0271	0.7017	0.6470	0.4068
Cluster	S19	S20	S21	S22	S23	S24	S25		
Positive ratio	0.1068	0.0200	0.6520	0.4806	0.1323	0.0523	0.0282		

The clustering results using SOM are reasonably good; however, it underperforms compared to the WISRnet. In the case of WISRnet, there are three clusters with a positive ratio larger than 90%, one cluster above 80%, and one at 64%.

The performance of the SOM approach may be improved by coupling it with a *K*-means clustering approach in conjunction with a Gaussian kernel-based convolution. Such an approach is beyond the scope of the present study.

REFERENCES

- Abadi, M., and Coauthors, 2016: Tensorflow: A system for large-scale machine learning. *12th USENIX Symp. on Operating Systems Design and Implementation*, Savannah, GA, USENIX, 265–283.
- Acuña-Escobar, D., M. Intrigo-Pazmiño, and J. Ibarra-Fiallo, 2022: Weather recognition using self-supervised deep learning. *SmartTech-IC 2021: Smart Technologies, Systems and Applications*, F. R. Narváez et al., Eds., Communications in Computer and Information Science, Vol. 1532, Springer, 161–174, https://doi.org/10.1007/978-3-030-99170-8_12.
- Agostinelli, F., M. Hoffman, P. Sadowski, and P. Baldi, 2014: Learning activation functions to improve deep neural networks. arXiv, 1412.6830v3, <https://doi.org/10.48550/arXiv.1412.6830>.
- Anantrasirichai, N., J. Biggs, F. Albino, P. Hill, and D. Bull, 2018: Application of machine learning to classification of volcanic deformation in routinely generated InSAR data. *J. Geophys. Res. Solid Earth*, **123**, 6592–6606, <https://doi.org/10.1029/2018JB015911>.
- Babar, B., R. Graversen, and T. Boström, 2019: Solar radiation estimation at high latitudes: Assessment of the CMSAF databases, ASR and ERA5. *Sol. Energy*, **182**, 397–411, <https://doi.org/10.1016/j.solener.2019.02.058>.
- Badrinarayanan, V., A. Kendall, and R. Cipolla, 2017: SegNet: A deep convolutional encoder-decoder architecture for image segmentation. *IEEE Trans. Pattern Anal. Mach. Intell.*, **39**, 2481–2495, <https://doi.org/10.1109/TPAMI.2016.2644615>.
- Bao, M., and J. M. Wallace, 2015: Cluster analysis of Northern Hemisphere wintertime 500-hPa flow regimes during 1920–2014. *J. Atmos. Sci.*, **72**, 3597–3608, <https://doi.org/10.1175/JAS-D-15-0001.1>.
- Cassano, J. J., P. Uotila, A. H. Lynch, and E. N. Cassano, 2007: Predicted changes in synoptic forcing of net precipitation in large Arctic river basins during the 21st century. *J. Geophys. Res.*, **112**, G04S49, <https://doi.org/10.1029/2006JG000332>.
- Chattopadhyay, A., P. Hassanzadeh, and S. Pasha, 2020a: Predicting clustered weather patterns: A test case for applications of convolutional neural networks to spatio-temporal climate data. *Sci. Rep.*, **10**, 1317, <https://doi.org/10.1038/s41598-020-57897-9>.
- , E. Nabizadeh, and P. Hassanzadeh, 2020b: Analog forecasting of extreme-causing weather patterns using deep learning. *J. Adv. Model. Earth Syst.*, **12**, e2019MS001958, <https://doi.org/10.1029/2019MS001958>.
- Cheneka, B. R., S. J. Watson, and S. Basu, 2021: Associating synoptic-scale weather patterns with aggregated offshore wind power production and ramps. *Energies*, **14**, 3903, <https://doi.org/10.3390/en14133903>.
- Cheng, X., and J. M. Wallace, 1993: Cluster analysis of the Northern Hemisphere wintertime 500-hPa height field: Spatial patterns. *J. Atmos. Sci.*, **50**, 2674–2696, [https://doi.org/10.1175/1520-0469\(1993\)050<2674:CAOTNH>2.0.CO;2](https://doi.org/10.1175/1520-0469(1993)050<2674:CAOTNH>2.0.CO;2).
- Davies, D. L., and D. W. Bouldin, 1979: A cluster separation measure. *IEEE Trans. Pattern Anal. Mach. Intell.*, **PAMI-1**, 224–227, <https://doi.org/10.1109/TPAMI.1979.4766909>.
- Denby, L., 2020: Discovering the importance of mesoscale cloud organization through unsupervised classification. *Geophys. Res. Lett.*, **47**, e2019GL085190, <https://doi.org/10.1029/2019GL085190>.
- Dong, G., G. Liao, H. Liu, and G. Kuang, 2018: A review of the autoencoder and its variants: A comparative perspective from target recognition in synthetic-aperture radar images. *IEEE Geosci. Remote Sens. Mag.*, **6**, 44–68, <https://doi.org/10.1109/MGRS.2018.2853555>.
- Dong, L., L. Wang, S. F. Khahro, S. Gao, and X. Liao, 2016: Wind power day-ahead prediction with cluster analysis of NWP. *Renewable Sustainable Energy Rev.*, **60**, 1206–1212, <https://doi.org/10.1016/j.rser.2016.01.106>.
- Esteves, J. T., G. de Souza Rolim, and A. S. Ferraudo, 2019: Rainfall prediction methodology with binary multilayer perceptron neural networks. *Climate Dyn.*, **52**, 2319–2331, <https://doi.org/10.1007/s00382-018-4252-x>.
- Fereday, D. R., J.R. Knight, A. A. Scaife, C. K. Folland, and A. Philipp, 2008: Cluster analysis of North Atlantic–European circulation types and links with tropical Pacific sea surface temperatures. *J. Climate*, **21**, 3687–3703, <https://doi.org/10.1175/2007JCLI1875.1>.
- Ferranti, L., S. Corti, and M. Janousek, 2015: Flow-dependent verification of the ECMWF ensemble over the Euro-Atlantic sector. *Quart. J. Roy. Meteor. Soc.*, **141**, 916–924, <https://doi.org/10.1002/qj.2411>.
- Francis, J., and N. Skific, 2015: Evidence linking rapid Arctic warming to mid-latitude weather patterns. *Philos. Trans. Roy. Soc.*, **A373**, 20140170, <http://doi.org/10.1098/rsta.2014.0170>.
- Gibson, P. B., S. E. Perkins-Kirkpatrick, P. Uotila, A. S. Pepler, and L. V. Alexander, 2017: On the use of self-organizing maps for studying climate extremes. *J. Geophys. Res. Atmos.*, **122**, 3891–3903, <https://doi.org/10.1002/2016JD026256>.
- Goodfellow, I., Y. Bengio, and A. Courville, 2016: *Deep Learning*. Adaptive Computation and Machine Learning Series, Vol. 1, MIT Press, 800 pp.
- Grotjahn, R., and Coauthors, 2016: North American extreme temperature events and related large scale meteorological patterns: A review of statistical methods, dynamics, modeling, and trends. *Climate Dyn.*, **46**, 1151–1184, <https://doi.org/10.1007/s00382-015-2638-6>.
- Gulli, A., and S. Pal, 2017: *Deep Learning with Keras*. Packt Publishing Ltd, 318 pp.
- Herman, G. R., and R. S. Schumacher, 2018: Money doesn't grow on trees, but forecasts do: Forecasting extreme precipitation with random forests. *Mon. Wea. Rev.*, **146**, 1571–1600, <https://doi.org/10.1175/MWR-D-17-0250.1>.
- Hersbach, H., and Coauthors, 2020: The ERA5 global reanalysis. *Quart. J. Roy. Meteor. Soc.*, **146**, 1999–2049, <https://doi.org/10.1002/qj.3803>.
- Hinton, G. E., and R. S. Zemel, 1994: Autoencoders, minimum description length, and Helmholtz free energy. *Advances in Neural Information Processing Systems 6*, J. D. Cowan, G. Tesauro, and J. Alspector, Eds., Morgan Kaufmann, 3–10.
- Horton, D. E., N. C. Johnson, D. Singh, D. L. Swain, B. Rajaratnam, and N. S. Diffenbaugh, 2015: Contribution of changes in atmospheric circulation patterns to extreme temperature trends. *Nature*, **522**, 465–469, <https://doi.org/10.1038/nature14550>.

- Jain, A. K., M. N. Murty, and P. J. Flynn, 1999: Data clustering: A review. *ACM Comput. Surv.*, **31**, 264–323, <https://doi.org/10.1145/331499.331504>.
- Jiang, X., and Coauthors, 2021: Rapid and large-scale mapping of flood inundation via integrating spaceborne synthetic aperture radar imagery with unsupervised deep learning. *ISPRS J. Photogramm. Remote Sens.*, **178**, 36–50, <https://doi.org/10.1016/j.isprsjprs.2021.05.019>.
- Jing, L., and Y. Tian, 2020: Self-supervised visual feature learning with deep neural networks: A survey. *IEEE Trans. Pattern Anal. Mach. Intell.*, **43**, 4037–4058, <https://doi.org/10.1109/TPAMI.2020.2992393>.
- Johnson, N. C., S. B. Feldstein, and B. Tremblay, 2008: The continuum of Northern Hemisphere teleconnection patterns and a description of the NAO shift with the use of self-organizing maps. *J. Climate*, **21**, 6354–6371, <https://doi.org/10.1175/2008JCLI2380.1>.
- Joseph, S., A. K. Sahai, R. Chattopadhyay, and B. N. Goswami, 2011: Can El Niño–Southern Oscillation (ENSO) events modulate intraseasonal oscillations of Indian summer monsoon? *J. Geophys. Res.*, **116**, D20123, <https://doi.org/10.1029/2010JD015510>.
- Kingma, D. P., and J. Ba, 2014: Adam: A method for stochastic optimization. arXiv, 1412.6980v9, <https://doi.org/10.48550/arXiv.1412.6980>.
- Kohonen, T., 1990: The self-organizing map. *Proc. IEEE*, **78**, 1464–1480, <https://doi.org/10.1109/5.58325>.
- , 2013: Essentials of the self-organizing map. *Neural Networks*, **37**, 52–65, <https://doi.org/10.1016/j.neunet.2012.09.018>.
- Kolesnikov, A., X. Zhai, and L. Beyer, 2019: Revisiting self-supervised visual representation learning. *Proc. IEEE/CVF Conf. on Computer Vision and Pattern Recognition*, Los Angeles CA, Institute of Electrical and Electronics Engineers, 1920–1929.
- Kotsiantis, S. B., I. Zaharakis, and P. Pintelas, 2007: Supervised machine learning: A review of classification techniques. *Proc. 2007 Conf. on Emerging Artificial Intelligence Applications in Computer Engineering*, Amsterdam, Netherlands, Association for Computing Machinery, 3–24.
- Krizhevsky, A., I. Sutskever, and G. E. Hinton, 2012: Imagenet classification with deep convolutional neural networks. *NIPS'12: Proceedings of the 25th International Conference Neural Information Processing Systems*, F. Pereira et al., Eds., Vol. 1, Curran Associates Inc., 1097–1105.
- LeCun, Y., Y. Bengio, and G. Hinton, 2015: Deep learning. *Nature*, **521**, 436–444, <https://doi.org/10.1038/nature14539>.
- Lee, S., and S. B. Feldstein, 2013: Detecting ozone- and greenhouse gas-driven wind trends with observational data. *Science*, **339**, 563–567, <https://doi.org/10.1126/science.1225154>.
- Li, B., S. Basu, S. J. Watson, and H. W. Russchenberg, 2020: Quantifying the predictability of a ‘Dunkelflaute’ event by utilizing a mesoscale model. *J. Phys. Conf. Ser.*, **1618**, 062042, <https://doi.org/10.1088/1742-6596/1618/6/062042>.
- , —, —, and —, 2021a: A brief climatology of Dunkelflaute events over and surrounding the north and Baltic Sea areas. *Energies*, **14**, 6508, <https://doi.org/10.3390/en14206508>.
- , —, —, and —, 2021b: Mesoscale modeling of a “Dunkelflaute” event. *Wind Energy*, **24**, 5–23, <https://doi.org/10.1002/we.2554>.
- Li, C., J. Wang, L. Wang, L. Hu, and P. Gong, 2014: Comparison of classification algorithms and training sample sizes in urban land classification with Landsat thematic mapper imagery. *Remote Sens.*, **6**, 964–983, <https://doi.org/10.3390/rs6020964>.
- Liu, Y., and Coauthors, 2016: Application of deep convolutional neural networks for detecting extreme weather in climate datasets. arXiv, 1605.01156v1, <https://doi.org/10.48550/arXiv.1605.01156>.
- Lloyd, S., 1982: Least squares quantization in PCM. *IEEE Trans. Inf. Theor.*, **28**, 129–137, <https://doi.org/10.1109/TIT.1982.1056489>.
- Loikith, P. C., B. R. Lintner, and A. Sweeney, 2017: Characterizing large-scale meteorological patterns and associated temperature and precipitation extremes over the northwestern United States using self-organizing maps. *J. Climate*, **30**, 2829–2847, <https://doi.org/10.1175/JCLI-D-16-0670.1>.
- McGovern, A., K. L. Elmore, D. J. Gagne, S. E. Haupt, C. D. Karstens, R. Lagerquist, T. Smith, and J. K. Williams, 2017: Using artificial intelligence to improve real-time decision-making for high-impact weather. *Bull. Amer. Meteor. Soc.*, **98**, 2073–2090, <https://doi.org/10.1175/BAMS-D-16-0123.1>.
- Meinke-Hubeny, F., L. P. N. de Oliveira, J. Duerinck, P. Lode-wijks, and R. Belmans, 2017: Energy transition in Belgium—Choices and costs. EnergyVille Tech. Rep., 35 pp., https://www.energyville.be/sites/energyville/files/downloads/2018/energyville_energy_transition_in_belgium_choices_and_costs_final_27apr2017_pverraturum_0_1.pdf.
- Neal, R., D. Fereday, R. Crocker, and R. E. Comer, 2016: A flexible approach to defining weather patterns and their application in weather forecasting over Europe. *Meteor. Appl.*, **23**, 389–400, <https://doi.org/10.1002/met.1563>.
- Ohba, M., S. Kadokura, and D. Nohara, 2016: Impacts of synoptic circulation patterns on wind power ramp events in east Japan. *Renewable Energy*, **96**, 591–602, <https://doi.org/10.1016/j.renene.2016.05.032>.
- Pedregosa, F., and Coauthors, 2011: Scikit-learn: Machine learning in Python. *J. Mach. Learn. Res.*, **12**, 2825–2830.
- Peng, B., Q. Huang, J. Vongkusolkiet, S. Gao, D. B. Wright, Z. N. Fang, and Y. Qiang, 2020: Urban flood mapping with bitemporal multispectral imagery via a self-supervised learning framework. *IEEE J. Sel. Top. Appl. Earth Obs. Remote Sens.*, **14**, 2001–2016, <https://doi.org/10.1109/JSTARS.2020.3047677>.
- Racah, E., C. Beckham, T. Maharaj, Prabhat, and C. Pal, 2016: Semi-supervised detection of extreme weather events in large climate datasets. arXiv, 1612.02095, <https://doi.org/10.48550/arXiv.1612.02095>.
- , —, —, S. Ebrahimi Kahou, M. Prabhat, and C. Pal, 2017: ExtremeWeather: A large-scale climate dataset for semi-supervised detection, localization, and understanding of extreme weather events. *NIPS'17: Proceedings of the 31st International Conference on Neural Information Processing Systems*, U. von Luxburg et al., Eds., Curran Associates Inc., 3405–3416.
- Ranzato, M., F. J. Huang, Y.-L. Boureau, and Y. LeCun, 2007: Unsupervised learning of invariant feature hierarchies with applications to object recognition. *2007 IEEE Conf. on Computer Vision and Pattern Recognition*, Minneapolis, MN, Institute of Electrical and Electronics Engineers, 1–8, <https://doi.org/10.1109/CVPR.2007.383157>.
- Rasp, S., and S. Lerch, 2018: Neural networks for postprocessing ensemble weather forecasts. *Mon. Wea. Rev.*, **146**, 3885–3900, <https://doi.org/10.1175/MWR-D-18-0187.1>.
- Sahai, A. K., N. Borah, R. Chattopadhyay, S. Joseph, and S. Abhilash, 2017: A bias-correction and downscaling technique for operational extended range forecasts based on self organizing

- map. *Climate Dyn.*, **48**, 2437–2451, <https://doi.org/10.1007/s00382-016-3214-4>.
- Shalev-Shwartz, S., and S. Ben-David, 2014: *Understanding Machine Learning: From Theory to Algorithms*. Cambridge University Press, 415 pp.
- Shi, C., C. Wang, Y. Wang, and B. Xiao, 2017: Deep convolutional activations-based features for ground-based cloud classification. *IEEE Geosci. Remote Sens. Lett.*, **14**, 816–820, <https://doi.org/10.1109/LGRS.2017.2681658>.
- Sianturi, Y., Marjuki, and K. Sartika, 2020: Evaluation of ERA5 and MERRA2 reanalyses to estimate solar irradiance using ground observations over Indonesia region. *AIP Conf. Proc.*, **2223**, 020002, <https://doi.org/10.1063/5.0000854>.
- Totz, S., E. Tziperman, D. Coumou, K. Pfeiffer, and J. Cohen, 2017: Winter precipitation forecast in the European and Mediterranean regions using cluster analysis. *Geophys. Res. Lett.*, **44**, 12 418–12 426, <https://doi.org/10.1002/2017GL075674>.
- Truys, J., and J. Vandervelden, 2017: België telde negen dagen Dunkelflaute in januari (Belgium had nine days of Dunkelflaute in January). *VRT News*, 24 February, https://www.vrt.be/vrtnws/nl/2017/02/24/belgie_telde_negendagendunkelflauteinjanuari-1-2900900/.
- Vettigli, G., 2018: MiniSom: Minimalistic and Numpy-based implementation of the self organizing map. GitHub, <https://github.com/JustGlowing/minisom/>.
- Vigaud, N., M. Ting, D.-E. Lee, A. G. Barnston, and Y. Kushnir, 2018: Multiscale variability in North American summer maximum temperatures and modulations from the North Atlantic simulated by an AGCM. *J. Climate*, **31**, 2549–2562, <https://doi.org/10.1175/JCLI-D-17-0392.1>.
- Wang, K., X. Qi, H. Liu, and J. Song, 2018: Deep belief network based *k*-means cluster approach for short-term wind power forecasting. *Energy*, **165**, 840–852, <https://doi.org/10.1016/j.energy.2018.09.118>.
- Wetzel, D., 2017: Die “dunkelflaute” bringt deutschland’s stromversorgung ans limit (The “dark lull” pushes Germany’s power supply to the limit). *Die Welt*, 2 June, <https://www.welt.de/wirtschaft/article161831272/Die-Dunkelflaute-bringt-Deutschlands-Stromversorgung-ans-Limit.html>.
- Xiao, H., F. Zhang, Q. He, P. Liu, F. Yan, L. Miao, and Z. Yang, 2019: Classification of ice crystal habits observed from airborne cloud particle imager by deep transfer learning. *Earth Space Sci.*, **6**, 1877–1886, <https://doi.org/10.1029/2019EA000636>.
- Xu, J., O. Schüssler, D. G. L. Rodriguez, F. Romahn, and A. Doicu, 2017: A novel ozone profile shape retrieval using Full-Physics Inverse Learning Machine (FP-ILM). *IEEE J. Sel. Top. Appl. Earth Obs. Remote Sens.*, **10**, 5442–5457, <https://doi.org/10.1109/JSTARS.2017.2740168>.
- Zanero, S., and S. M. Savaresi, 2004: Unsupervised learning techniques for an intrusion detection system. *SAC’04: Proc. 2004 ACM Symp. on Applied Computing*, New York, NY, Association for Computing Machinery, 412–419.
- Zhang, J., P. Liu, F. Zhang, and Q. Song, 2018: Cloudnet: Ground-based cloud classification with deep convolutional neural network. *Geophys. Res. Lett.*, **45**, 8665–8672, <https://doi.org/10.1029/2018GL077787>.